Applied Thermal Engineering 235 (2023) 121281

Contents lists available at ScienceDirect

Applied Thermal Engineering

journal homepage: www.elsevier.com/locate/ate

Research Paper

Parameter study for oil spray cooling on endwindings of electric machines via Eulerian–Lagrangian simulation

An Zhao [a,*], Christophe Duwig [b], Chuan Liu [c], David Gerada [c], Mats Leksell [a]

[a] Department of Electrical Power and Energy Systems, KTH Royal Institute of Technology, Stockholm, Sweden
[b] Department of Chemical Engineering, KTH Royal Institute of Technology, Stockholm, Sweden
[c] Faculty of Engineering, University of Nottingham, Nottingham, United Kingdom

ARTICLE INFO

Keywords:
Spray cooling
CFD simulation
DPM
Multi-nozzles
Endwindings
Electric machines

ABSTRACT

The demand for larger power density and torque for the power traction motors used in electrified transportation puts forward a requirement for better thermal management methods. Spray cooling is a promising direct liquid cooling technique that has been proved to possess high heat removal capability in previous research. This paper investigates the heat transfer characteristics of spray cooling on endwindings of electric machines via numerical simulation through an Eulerian–Lagrangian approach. The utilized numerical models and calculated results are validated with experimentally measured data. The influence of different parameters and options involved in the simulation settings on the final results, like the stream numbers for the spray injector, the constant heat flux versus constant temperature thermal boundary condition, the influence of splashing, the effect of heat conduction in the endwindings and the Saffman lift force, only solving the energy equation for the air after its flow field reaches a steady-state, are evaluated. Parameter analyses are also conducted for operation conditions, configuration of the spray nozzles, and material properties of the coolant liquid. It is found that larger flow rate, smaller droplet size, lower spray height, more nozzle numbers, larger thermal conductivity and smaller viscosity of the coolant liquid tend to increase the overall heat transfer performance.

1. Introduction

The ongoing electrification for transportation, in particular, electric vehicles (EV) [1] and more electric aircrafts (MEA) [2], answers the decarbonization of transport in general [3]. Electric machines are one of the core components in drives for these vehicles. Minimizing the production cost and maximizing the power and torque density are two key objectives to achieving high-performance electric vehicles and enabling rapid deployment. To that end, the design procedure of these electric machines must be thought through using innovations and detailed designs. One important feature is the use of hairpin windings that are gaining popularity in the industry. This technology reduces the manufacturing time because they can be produced via an automatic assembly line [4], instead of wrapping all the copper coils manually as for the conventional random windings. Hairpin windings also provide a larger slot fill factor owing to their rectangular shapes [5]. It enables to fit the stator slots better and need fewer impregnation materials in between, making the units cheaper to produce. Compared to the common random windings, they can achieve higher stator currents to enable larger power and torque density in the machines. Hairpin windings have been already adopted by several actors, such as Remy International [6] and Toyota [7], and may become a dominant technology in automotive industry.

As an integrated part of the design, avoid overheating will focus on cooling the machine to secure optimal operation. Forced air convection [8] and liquid jacket cooling [9] are two widely adopted thermal management methods in commercialized (often steady-state operation) electric machines. EVs operate transiently with high peaks at acceleration and braking. In order to dissipate the heat generated by those power traction motors in a limited enclosure, a cooling capability as large as several kilowatts per kilograms of the machine [10] is needed, which is challenging for conventional thermal management methods. Spray cooling is a promising new cooling scheme that has been proved to possess heat removal flux as high as tens of W/cm^2 [11], and has already found its applications in cooling of high-power light emitting diodes (LED) chips [12,13] and power electronics devices used in EVs or MEAs [14]. The concept is similar to jet impingement cooling

* Corresponding author.
E-mail address: azhao@kth.se (A. Zhao).

https://doi.org/10.1016/j.applthermaleng.2023.121281
Received 21 February 2023; Received in revised form 10 July 2023; Accepted 2 August 2023
Available online 18 August 2023

Nomenclature

A_c	Cell surface area [m^2]
A_d	Spray droplet surface area [m^2]
A_w	Wall surface area [m^2]
A_{wp}	Wall-film parcel area [m^2]
C_f	Drag coefficient at the liquid-gas interface [$kg/(m^2\ s)$]
c_{pg}	Specific heat capacity of the gas phase under constant pressure [W/(kg K)]
c_{pl}	Specific heat capacity of the liquid phase under constant pressure [W/(kg K)]
D_{32}	Sauter mean diameter of the spray droplet size distribution [m]
D_p	Diameter of the spray droplet [m]
$\vec{g}$	Gravity acceleration [m^2/s]
H	Wall-film thickness [m]
h_g	Specific enthalpy of the gas phase [J/kg]
k	Specific turbulence kinetic energy [m^2/s^2]
k_g	Gas thermal conductivity [W/(m K)]
k_l	Liquid thermal conductivity [W/(m K)]
L_{wd}	Radial width of the endwindings [m]
L_{wp}	Characteristic length of the wall-film parcel [m]
m_{film}	Mass of the wall-film [kg]
m_p	Mass of the spray parcel [kg]
m_{wp}	Mass of the wall-film parcel [kg]
$\overline{P}_g$	RANS averaged pressure of the gas phase [Pa]
$\dot{q}_w$	Wall heat flux [W/m^2]
t	Time [s]
T_g	Bulk gas phase temperature [°C]
T_p	Spray parcel temperature [°C]
T_s	Wall-film surface temperature [°C]
T_{wp}	Wall-film parcel temperature [°C]
$\vec{\overline{u}}$	RANS averaged Velocity of the gas [m/s]
u_g	Characteristic air velocity near the surface of endwindings [m/s]
u_i	Gas velocity along the ith coordinate axis [m/s]
$\overrightarrow{u_p}$	Velocity of the spray parcel [m/s]
$u_{p,i}$	Spray droplet velocity along the ith coordinate axis [m/s]
u_{pn}	Spray droplet velocity normal to the wall [m/s]
$\overrightarrow{u_{wp}}$	Velocity of the wall-film parcel [m/s]
V_{wp}	Volume of the spray parcel [m/s]
x_i	Position along the ith coordinate axis [m]
Y	Fraction of the droplets whose diameter is smaller than D_p [-]
ε	Specific turbulence dissipation rate [m^2/s^3]
μ_g	Gas dynamic viscosity [kg/(m s)]
μ_l	Liquid dynamic viscosity [kg/(m s)]
ν_g	Gas kinetic viscosity [m^2/s]
ρ_g	Gas density [kg/m^3]
ρ_l	Liquid density [kg/m^3]
σ	Surface tension [N/m]

— using nozzles to inject coolant fluids directly onto the heated surface. While compared to air jet impingement, oil spray cooling is capable of providing similar heat transfer performance with a smaller mass flow rate of coolant, at a cost of more advanced injectors [15]. By establishing a closed loop for spray cooling, it is possible to realize continuous high heat removal flux as well [16]. Numerous parameter studies concerning the nozzle positioning [17], coolant volumetric flow rate [18], heated surface roughness [19], types of heating surface [20], types of additives [21], etc., were also conducted in the spray cooling research community through both the experiments [22] and numerical simulation [23].

Endwindings in electric machines are suitable targets to apply direct spray cooling on [24] as the direct contact between the non-conducting coolant droplets and the surface of endwindings. This scheme transfers heat more efficiently than alternative strategies, such as forced air convection or liquid jacket cooling. Recent research is therefore looking at implementing different practical configurations of spray cooling for power traction motors. For example, Davin, et al. [25] in 2015 investigated the cooling performance of oil injected from the top of the endwindings in electric machines with lubricating oil as the coolant. Four different injection patterns, full cone nozzle, flat jet nozzle, dripping, and multi-jets, are tested with the oil flow rate, oil temperature, and rotor speed varied between 40 to 120 L/h, 50 to 75 °C and 0 to 4600 rpm, respectively. They found that the oil flow rate is the main factor for global cooling efficiency, while the rotation speed does not enhance the global cooling efficiency but helps redistribute oil in the domain and affects the local temperature distribution. Lim and Kim [26] in 2014 developed an oil spray cooling system for in-wheel motors by supplying the coolant oil through a hollow shaft and ejecting it by virtue of the centrifugal force. The shape of the cooling channel was optimized based on the Taguchi method to improve the thermal response of the stator windings and the stator yoke. The temperature of stator windings under the continuous rating driving conditions was lowered below the temperature limit of 150 °C via this spray cooling setup, and it can be further reduced by increasing the oil flow rate or decreasing the oil temperature. Park and Kim [27] extended this work in 2019 by conducting the computational fluid dynamics (CFD) numerical simulation for this spray cooling setup. They made the experimental results and simulation results consistent within 2.1% error and confirmed the effectiveness of this spray cooling system. Moreover, they found that the cooling effect due to the oil film and secondary flow, indicated by a Nusselt number, increases 9.8 times at the maximum speed of 11 000 rpm compared to the base speed of 4400 rpm.

The University of Nottingham and MotorDesign Ltd. collaborated in carrying out a series of research on the topic of spray cooling for hairpin windings. In 2019 Liu, et al. [28] built a test bench with 72-slot, 2-layer hairpin windings and three types of spray nozzles installed in parallel to the axial axis of the endwindings. They affixed 24 type-K thermocouples onto the drive end surface of these hairpin windings and observed a nonuniform temperature distribution along the circumferential direction. Such temperature ununiformness can be mitigated by increasing the spray angle, the number of spray nozzles, or increasing the oil flow rate. For cooling efficiency, they discovered that it would be better by using designs with a higher number of low-flow-rate nozzles compared to designs with a lower number of high-flow-rate nozzles, and the two types of solid-cone nozzles are generally better than the hollow-cone type nozzle. In 2020 Chong et al. [29] modified this test bench by changing the spray nozzles to the radial direction at 9 o'clock, 12 o'clock, and 3 o'clock positions. Another misting type nozzle was tested as well and was found to give similar cooling efficiency as solid-cone nozzles but better temperature n along the circumferential direction than them. They also observed that the oil film falling due to the gravitational force is enough to wet and cool the lower part of the endwindings. A similar conclusion has also been drawn by Davin et al. [25]. Liu, et al. established a reduced model for predicting the heat transfer coefficient (HTC) of oil spray cooling on hairpin windings in 2020 [30]. They pointed out that it is crucial to use the suitable definition of heat exchange surface area in calculating the HTC. The method based on the surface area of individual wires (AS) described

in their article is considered to be most appropriate for comparing the calculated HTCs with other works, especially with CFD simulation results. The rectified HTCs for the experimental results in [28] using this heat exchange area are recently published in [31].

In contrast to a relatively large number of studies focusing on experimental spray cooling on the endwindings in electric machines, there is only a limited amount of studies focusing on simulations. Several noteworthy works according to the limited knowledge of authors are as follows: Beck et al. [32] utilized the volume of fluid (VoF) method [33] combined with the large-eddy simulation (LES) turbulence model to simulate the flow inside the nozzle before the formation of spray. Those nozzles are actually stepped holes opened on a hollow shaft. They observed different cross-section shapes of the jet at the nozzle exist, which is mainly determined by the ratio of the impingement momentum and the counteracting Coriolis force. Unfortunately, until now such interface-resolving methods are still too time-consuming and computationally expensive for simulating the complete spray cooling process. Ha et al. [34] utilized the moving particle simulation (MPS) method [35] to simulate the formation rate of the oil film on the hairpin windings accumulated from the spray injected from the dripping nozzles or solid-cone nozzles. They found that the dripping nozzles result in less splashing and thicker oil film than the solid-cone nozzles, which should offer higher heat removal capacity. However, the heat transfer process is not included in their simulation. La Rocca, et al. [36] utilized the discrete phase model (DPM) in a pseudo-transient approach for simulating the spray cooling heat transfer process on a 60° sector of two-layer hairpin windings, which is proved to significantly reduce the computing time from the order of weeks for a full transient approach to a few days. They found that the temperature difference could be as large as 70 °C between the coolest part and the hot spot, and the averaged HTC is around 400 W/(m^2 K). The same authors [37] applied the same approach on a 60° sector of another eight-layer hairpin windings. They found that the penetration of spray droplets is limited by the large number of conductors and this makes some conductors stay dry during the simulation. In addition, the layout of nozzles turns out to be a big factor affecting the overall cooling performance, changing the position leads to over 20% variation of the averaged HTC.

While these computational studies have shown potential, there is still a knowledge gap regarding the influence of different simulation settings for the DPM on the results of the spray cooling heat transfer on the endwindings. It limits the applicability in industry and needs to be addressed for enabling virtual design of electrical machines. Therefore, the present work aims at investigating the detailed aspects of the DPM for simulating the spray cooling heat transfer on endwindings of electric machines and then investigating the parameters that are difficult to measure or change in the experiments but are central to the heat transfer performance of the spray cooling process. The outline of this paper is as follows: The numerical models used for simulating the movement of the air, spray droplet, the thin liquid film formed on the wall surface, and the energy transfer among them, are introduced in Section 2. The simulation settings of applying these numerical models to a multi-nozzle spray cooling configuration on a simplified geometry of endwindings are described in Section 4. Then a detailed study about the influence of different aspects of the simulation settings on the results is done in Section 5. Sensitivity analyses are conducted for vital parameters of the spray cooling heat transfer on endwindings of electric machines in Section 6. Finally, conclusions are drawn in Section 7.

2. Numerical models

The numerical models used for simulating the two-phase flow and heat transfer mechanisms of spray cooling are based on the Eulerian–Lagrangian framework. The continuous gas phase, air, is solved in the Eulerian coordinates while the dispersed liquid phase, coolant droplets, is solved in the Lagrangian coordinates. These two phases can exchange mass, momentum, and energy with each other.

2.1. Governing equations of continuous gas phase

Sprays are generally a turbulent process [38]. Hence, the governing equations of the continuous gas phase, air, are Reynolds-averaged Navier–Stokes equations. The mass conservation equation is written as

$$\frac{\partial \rho_g}{\partial t} + \frac{\partial(\rho_g \bar{u}_i)}{\partial x_i} = S_m. \tag{1}$$

where S_m denotes the coupling mass source term transferred from the dispersed liquid phase, which is set to 0 if the evaporation of spray droplets is neglected. This approximation is made according to the test data from the datasheet of the coolant liquid, Eastman Turbo oil 2389, used in this work [39]. The measured evaporation loss, complying with the standard ASTM D 972 [40], of this oil after 6.5 h under 205 °C temperature is 20%. But the temperature of the air in the endcap region of electric machines is usually below 100 °C and the residence time of the coolant liquid in it is just a few seconds. Furthermore, the vapor pressure for typical lubricant oil at a temperature as high as 120 °C is merely at a level of 2 Pa [41], meaning in the worst scenario the saturated vapor evaporated from the oil wall-film would be just 20 ppm of the air in the endcap of the electric machines. Therefore, the neglect of the evaporation effect of spray droplets is justified.

The momentum conservation equation is written as

$$\frac{\partial \rho_g \bar{u}_i}{\partial t} + \frac{\partial(\rho_g \bar{u}_i \bar{u}_j)}{\partial x_j} = -\frac{\partial \overline{P}_g}{\partial x_i} + \frac{\partial}{\partial x_i}((\mu_g + \mu_t)\frac{\partial \bar{u}_i}{\partial x_j}) + \rho_g g_i + S_{u_i}. \tag{2}$$

Here μ_t denotes the turbulence viscosity, calculated as

$$\mu_t = C_\mu \rho_g \frac{k^2}{\epsilon} \tag{3}$$

where the turbulence kinetic energy k and the turbulence dissipation rate ϵ are obtained from solving a two-equation model for turbulent flows. S_{u_i} is the coupling momentum source term transferred from the dispersed liquid phase, calculated as

$$S_{u_i} = \sum_{p}^{N_{c,parcel}} [m_p(\frac{u_{p,i} - \bar{u}_i}{\tau_t}) + F_{extra,i}] \tag{4}$$

where $N_{c,parcel}$ denotes the total number of spray parcels in the cell. Other notations related to the dispersed liquid phase are described later in Section 2.2.

The energy conservation equation is written as

$$\begin{aligned} &\frac{\partial(\rho_g(h_g + \frac{1}{2}\bar{u}_i\bar{u}_i))}{\partial t} + \frac{\partial(\rho_g \bar{u}_i(h_g + \frac{1}{2}\bar{u}_i\bar{u}_i))}{\partial x_i} = \\ &\frac{\partial P_g}{\partial t} + \frac{\partial}{\partial x_i}((k_g + \frac{c_{pg}\mu_t}{Pr_t})\frac{\partial T_g}{\partial x_i}) + \rho g_i \bar{u}_i + S_h \end{aligned} \tag{5}$$

where Pr_t denotes the turbulent Prandtl number, which is chosen to be 0.85 at the wall [42]. S_h is the coupling energy source term transferred from the dispersed liquid phase, calculated as

$$S_h = \frac{\sum_p^{N_{c,parcel}} [m_p c_{pl}(T_{p,in} - T_{p,out})]}{\Delta t_p} \tag{6}$$

where ΔT denotes the DPM time step, $T_{p,in}$ and $T_{p,out}$ are the temperature of the spray parcels entering and leaving the cell, respectively. Source terms in Eqs. (1), (2) and (5) are linearized to enhance the stabilization of the solution.

It has been proved in previous research [23,43] of spray cooling that adopting the Realizable k-ϵ model [44] as the turbulence model is a good compromise between the computational accuracy and computational cost. Hence, it is also employed in this work.

2.2. Governing equations of dispersed liquid phase

The dispersed liquid phase consists of a huge amount of spray droplets. In order to facilitate tracking the movement and energy transfer of all these spray droplets, those spray droplets with similar

positions, sizes, and velocities are lumped into one parcel [45]. These parcels are treated as infinitesimal points in the fluid domain, on the assumption that their volume is negligible compared to the cell volume where they locate in. The mass balance, force balance, and energy balance equations are then solved for each spray parcel instead of each spray droplet, which helps significantly reduce the required memories and computing time.

As mentioned in Section 2.1, the vaporization effect of spray droplets is neglected. Hence, except for the special cases in which the spray droplet secondary breakup submodel [46] or the stochastic collision submodel [47], the mass of each free spray parcel stays constant owing to its Lagrangian nature and no mass balance equation needs to be explicitly solved.

The trajectories of the spray particles when they are moving through the air are governed by the force balance as

$$m_p \frac{d}{dt}\vec{u_p} = m_p \frac{\vec{\bar{u}} - \vec{u_p}}{\tau_r} + m_p \frac{\vec{g}(\rho_p - \rho_g)}{\rho_p} + \vec{F_{extra}} \tag{7}$$

where the first term on the right-hand side of Eq. (7) is the drag force, the second term is the buoyancy force and the third term contains other extra forces, for example, the Saffman lift force [48]. Here τ_r is the droplet relaxation time [49], which is calculated by

$$\tau_r = \frac{\rho_l D_p^2}{18\mu_l} \frac{24}{C_D Re_{rel}} \tag{8}$$

where Re_{rel} denotes the relative Reynolds number defined on the basis of the droplet diameter and the difference between the droplet velocity and the gas phase velocity, $\frac{\rho_l D_p |\vec{u_p} - \vec{\bar{u}}|}{\mu_g}$. The drag coefficient C_D is computed via the classical correlation developed by Morsi and Alexander [50] for spherical particles with their relative Reynolds number between 0.1 and 50 000, including the range of relative Reynolds number of spray droplets in this work, 1 to 2000.

$$C_D = \frac{a_1}{Re_{rel}^2} + \frac{a_2}{Re_{rel}} + a_3 \tag{9}$$

where a_1, a_2 and a_3 are constant coefficients over a range of Re_{rel}. Their specific values are given in the appendix of [50]. The positions and velocities of all the free spray parcels are updated each DPM time step according to the discretized version of Eq. (7).

The inert heating or cooling of the spray droplets when they are moving through the air is governed by the energy balance as

$$m_p c_{pl} \frac{d}{dt} T_p = h_c A_d (T_g - T_p) \tag{10}$$

where h_c denotes the convection heat transfer coefficient used for calculating the heat transfer between the gas phase and the spray droplet. Its corresponding Nusselt number Nu_c, which is defined on the basis of the droplet diameter and the thermal conductivity of the gas phase, is estimated according to the Ranz correlation [51].

$$Nu_c = 2.0 + 0.6 Re_{rel}^{1/2} Pr_g^{1/3}. \tag{11}$$

The temperatures of all the free spray parcels are updated each DPM time step according to the discretized version of Eq. (10).

2.2.1. Droplet size distribution

Rosin-Rammler distribution is a widely used function for describing the droplet size distribution of sprays [52]. It is also adopted in this work and can be written as

$$1 - Y = \exp(-(D_p/\bar{D})^n) \tag{12}$$

Here $\bar{D}$ is called the characteristic diameter and has the following relationship with the Sauter mean diameter (SMD) [52],

$$\bar{D} = D_{32} \Gamma(1 - \frac{1}{n}) \tag{13}$$

where $\Gamma(\cdot)$ denotes the gamma function. The Rosin-Rammler distribution parameter n is chosen to be 3.5 in this work. Nevertheless, it is found by the authors later that changing it to 2.5 and 5.0 has a relatively small influence on the final results compared to other important parameters investigated in this work.

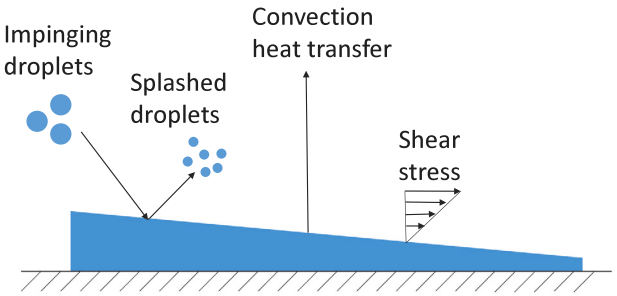

Fig. 1. The schematic of the Lagrangian wall-film model.

2.2.2. Lagrangian wall-film model

In this work, the interaction between the spray droplets and the wall of endwindings is modeled by the Lagrangian wall-film model [53], as illustrated in Fig. 1. Its basic assumption is that the wall-film thickness is much smaller than the radius of curvature of the wall surface. Hence, the wall-film velocity is always parallel to the wall surface and variation of physical properties across the wall-film is neglected. When a free spray parcel impinges upon the wall, it is converted into a wall-film parcel. During the conversion, the position of the parcel, the mean temperature of the parcel and the volume occupied by the parcel retain the same values. Similar to the free spray parcels, the physics of wall-film parcels are described and solved by the law of mass, momentum and energy conservation as well. But the mass conservation equation for the wall-film does not need to be explicitly solved as it is automatically satisfied owing to the Lagrangian nature of the wall-film parcels.

The momentum conservation equation for the wall-film is

$$\rho_l H \frac{d}{dt}\vec{u_{wp}} = \vec{\tau_g} - \vec{\tau_w} + \rho_l H \vec{g} \tag{14}$$

where H is the wall-film thickness of the specific cell the current wall-film parcel locates in, which is obtained by diving the sum of the wall-film parcel volumes in that cell with the cell face area.

$$H = \frac{\sum_{p=1}^{N_{c,parcel}} V_{wp}}{A_c} \tag{15}$$

$\vec{\tau_g}$ denotes the shear stress of the gas flow applied on the surface of the wall-film, which is calculated with the assistance of the solution of the continuous phase.

$$\vec{\tau_g} = C_f(\vec{\bar{u}} - 2\vec{u_{wp}}) \tag{16}$$

$\vec{\tau_w}$ denotes the wall stress, whose expression is derived based on the assumption that the velocity profile in the wall-film varies linearly with the distance from the wall, as the wall-film is very thin.

$$\vec{\tau_w} = \frac{\mu_l}{H/2}\vec{u_{wp}} \tag{17}$$

All the vectors in Eq. (14) are already projected onto the wall-tangential surface, as it is assumed that the ultimate effect of all the normal forces is merely to ensure the wall-film resides on the wall surfaces, i.e., the wall-normal component of the wall-film parcel velocity u_{wp} is explicitly forced to be zero at each DPM marching time step. The positions and velocities of all the wall-film parcels are updated according to the discretized version of the above-mentioned momentum conservation equation.

The energy conservation equation for the wall-film is given as

$$\frac{d}{dt}(m_{wp} c_{wp} T_{wp}) = Q_{wp,cond} + Q_{wp,conv} \tag{18}$$

where $Q_{wp,cond}$ denotes the heat transferred from the wall to the wall-film parcels. If the thermal boundary condition for the wall is constant temperature, it is defined as

$$Q_{wp,cond} = \frac{k_l A_{wp}}{H/2}(T_w - T_{wp}) \tag{19}$$

while if the thermal boundary condition for the wall is constant heat flux, it is defined as

$$Q_{wp,cond} = \dot{q}_w A_{wp}. \tag{20}$$

Here A_{wp} denotes the wall-film parcel area that is taken to be a mass-weighted percentage of the wall surface area, and $Q_{wp,conv}$ denotes the heat transferred from the wall-film to the gas phase. It is calculated as

$$Q_{wp,conv} = h_{wp,conv} A_{wp} (T_g - T_s) \tag{21}$$

where $h_{wp,conv}$ denotes the corresponding heat transfer coefficient, which is defined as

$$h_{wp,conv} = Nu_{wp,conv} k_g / L_{wp} \tag{22}$$

Here L_{wp} denotes the characteristic length of the wall-film parcel that is computed as the square root of the wall-film parcel area, and $Nu_{wp,conv}$ denotes the corresponding Nusselt number, which is predicted based on the following correlation equations.

$$\begin{aligned} Laminar\,flow &: Nu_{wp,conv} = 0.332 Re_{wp,conv}^{1/2} Pr_g^{1/3} \\ Turbulent\,flow &: Nu_{wp,conv} = 0.0296 Re_{wp,conv}^{4/5} Pr_g^{1/3} \end{aligned} \tag{23}$$

Here the Reynolds number $Re_{wp,conv}$ is defined on the basis of the wall-film parcel characteristic length, L_{wp}, and the wall-film parcel velocity, u_{wp}. The wall-film surface temperature T_s is calculated using the energy conservation equation on the interface.

$$h_{wp,conv}(T_g - T_s) = \frac{k_l}{H/2}(T_s - T_{wp}) \tag{24}$$

Due to the same reason mentioned in Section 2.1, the film vaporization and boiling effects are not taken into consideration. The temperatures of all the wall-film parcels are updated according to the discretized version of the above-mentioned energy conservation equation. During the solution, the heat balance between the power loss generated in the endwindings and the heat taken away by the coolant liquid is checked. It is done by comparing the applied heat dissipation rate on the surface of the endwindings and the total enthalpy change rate of all the wall-film parcels. Their difference turns out to be always lower than 0.3%.

The Stanton-Rutland model [54] is utilized to model the interaction between the spray droplets and the wall/wall-film, and the Friedrich model [55] is utilized to model the separation of the thin liquid film at a sharp corner of the wall. Details about them can be found in the supporting information of this paper. When needed, the TAB method [46] is utilized to model the secondary breakup of the spray droplets, and the collision among spray droplets is modeled in a stochastic way [47]. Readers are referred to these original articles for details of these two submodels.

2.3. Metric of the solution

Area-weighted averaging, Eq. (25), is used to extract the representative value for a quantity ϕ, such as the wall temperature, wall-film temperature, wall-film thickness, wall-film velocity magnitude, etc., on a specific wall surface.

$$\phi_{ave} = \frac{1}{A_t}\int \phi dA = \frac{1}{A_t}\sum_{j=1}^{N_{s,cells}} \phi_j A_j \tag{25}$$

Here $N_s, cells$ denotes the number of cell faces, ϕ_j indicates the quantity value on jth cell surface, A_j indicates the jth cell face area and A_t is the total area of this specific surface.

A total heat transfer coefficient is adopted as an overall metric for evaluating the spray cooling heat transfer performance in a specific case.

$$h_{tot} = \frac{q}{T_{w,ave} - T_{ref}} \tag{26}$$

Table 1
Parameters of the nozzle for single-nozzle spray cooling on a heated plate.

Parameter name	Unit	Value
Spray angle	°	68
Nozzle diameter	mm	0.61
Nozzle pressure drop	bar	2
Flow rate	kg/s	0.00382
Nominal outlet velocity	m/s	13.1

Here $T_{w,ave}$ denotes the area-weighted averaged wall temperature. T_{ref} is picked in a similar way as in [28], the temperature of the spray at the nozzle outlet, to be beneficial in comparing their experimental results.

Moreover, in order to quantify the degree of nonuniformity for the spray cooling heat transfer process on the surface of endwindings, two additional metrics, in the form of the relative standard deviations for the wall temperature and wall-film thickness distribution, are developed. They are simply defined as the percentage of their absolute standard deviations over the surface of endwindings divided by the corresponding area-weighted averaging values of them, respectively.

3. Verification with single-nozzle spray cooling experimental result

The feasibility and accuracy of these numerical models in simulating the spray cooling heat transfer process are verified with the result from a single-nozzle spray cooling experiment case [56]. Its configuration is a single spray nozzle placed at the top, 100 mm over a 20 × 20 mm^2 square heating plate. It is the solid-cone type and its main parameters are listed in Table 1. The Sauter mean diameter of the injected spray droplets from it is measured to be 0.061 mm. The fluid domain is meshed with 2.5 million structured hexagonal cells, with a minimum angle larger than 85° and a minimum orthogonal quality larger than 0.9. Constant heat flux 10 kW is applied on the heated wall surface and its DPM boundary condition is set to the "wall-film" type. Pressure-inlet is set for the ceiling and pressure-outlet is set for the four sides. All of them have gauge pressure values of zero and the "escape" type DPM boundary condition. Liquid water is used as the coolant liquid and air at atmospheric pressure is considered the continuous gas phase. Their material properties are set according to the appendix of [57]. The temperature of water at the nozzle outlet is 292 K and the ambient air temperature is 289 K. The same continuous phase and DPM solver settings as described in the main text. Fig. 2 illustrates the traces of spray droplets injected from the nozzle. They are colored by the DPM volume fraction, which is the discrete phase volume fraction within each cell. It is found that except for the region near the nozzle outlet and over the heated wall surface, the DPM volume fraction is always smaller than 1%, satisfying the basic assumption of the Eulerian–Lagrangian framework, verifying the feasibility of using the Eulerian–Lagrangian framework to simulate the two-phase flow mechanism of spray cooling.

Before the spray droplets reach the heating plate, the heat generation of the plate is deactivated, viz., its heat flux is set to 0 W/(m^2 K), for preventing its wall temperature value from reaching an unrealistic high value at the beginning. The wall temperature and wall-film thickness on the heated wall surface are monitored to judge if the steady-state is reached, which takes 320 ms after the spray droplets reach the heating plate. After the solution, the residuals of the energy equation decrease below 10e−5; the residuals of the continuity equation decrease below 10e−2; and the residuals of all other equations decrease below 10e−3, which indicates the convergence of the solution. The obtained DPM volume fraction, which is the discrete phase volume fraction within each cell, is found to be always smaller than 1% except for the region near the nozzle outlet and over the heated wall surface. This satisfies the basic assumption introduced in Section 2.2, verifying the feasibility of using the Eulerian–Lagrangian approach to simulate the two-phase ow mechanism of spray cooling. The final area-averaged

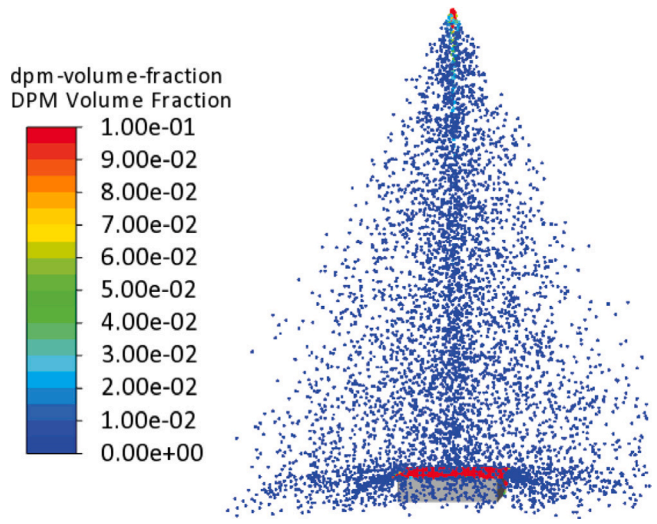

Fig. 2. Traces of droplets colored by the DPM volume fraction for the single-nozzle spray cooling simulation.

wall-film thickness over the heated wall surface is 83 μm, and the wall temperature of it is 311.5 °C, which is quite close to the experimentally measured value [56], 311.2 °C. Hence, the accuracy of the numerical models in simulating the spray cooling heat transfer process is also verified.

4. Simulation settings for spray cooling on endwindings

The present work adopts the axial-direction spray cooling configuration as in [28] for endwindings of electric machines. It is selected because it is among the earliest and most detailed research for the topic of applying spray cooling on endwindings in electric machines. Table 3 gives the main parameters for the nozzles used to generate the spray. Their injected sprays are in the form of solid cones. Four spray nozzles located 35 mm over the surface of endwindings are picked to be the baseline arrangement. The arrangement of these nozzles is shown in Fig. 3(a), they are distributed with uniformly spaced angles along the circumferential direction and their injection direction is parallel to the axial axis of the endwindings. The Eastman turbo oil 2389 [39] is adopted as the coolant liquid, whose physical properties are listed in Table 2. Same continuous phase and DPM solver settings as described in Section 3 are used here.

The fluid domain used in the CFD simulation is illustrated in Fig. 4(a). Its shape and dimension are modeled to be the same as the inner space inside the cylindrical perspex covers that imitate the endcap region of electric machines. Except these Perspex covers enclose the fluid domain as its ceiling and side walls, the bottom of the fluid domain is also the surface of the dummy rotor or the stator yoke. There is a tiny hole for dripping the coolant liquid in the lower region of the cylindrical Perspex covers but it is not modeled. Hence, the whole fluid domain is in fact completely confined by solid walls, namely, it has no inlets or outlets. The "trap" type DPM boundary condition is set for these walls to immediately terminate the tracking of the spray droplets when they hit these walls, preventing the waste of computing resources on them because they are probably not going to influence the heat transfer performance over the surface of endwindings anymore.

For the sake of significantly reducing the cell numbers and the computational cost, a simplified half-bagel-shaped geometry model is used to represent the endwindings in electric machines. Its surface is shown in Fig. 4(a), colored in orange, and its detailed geometrical dimensions are chosen to be the same as the one used in [30]. The "wall-film" type DPM boundary condition is set for it. A comparison of

Table 2
Material properties of Eastman Turbo oil 2389 [39].

Property name	Unit	Value
Density	kg/m^3	951
Viscosity	Pa s	0.0118
Specific thermal capacity	J/(kg K)	1859
Thermal conductivity	W/(m K)	0.151
Surface tension	N m	0.03[a]

[a]Due to the lack of surface tension data in the datasheet of this oil, a typical value for other oil [60] is used in this work. The sensitivity of spray cooling heat transfer performance caused by the change of its value will be discussed in Section 6.

Table 3
Parameters of the nozzles for spray cooling on endwindings under the reference operation condition.

Parameter name	Unit	Value
Spray angle	°	60
Nozzle diameter	mm	0.91
Nozzle pressure drop	bar	4.3
Flow rate	L/min	3.9
Nominal outlet velocity	m/s	25.1

such a simplified geometry model with a more realistic geometry model for endwindings has been done in [58] for forced air convection heat transfer analysis, and they found that the deviation of heat dissipation rate for the two models is as large as 62%. This number should be borne in mind when comparing the simulation results with the experimental results.

At last, in order to further decrease the cell numbers and the computational cost, the fluid domain is halved with a vertical plane. It is noted that there are two spray nozzles located exactly on the border of this symmetrical plane. This does not influence the final steady-state results, because after long enough iterations, statistically, 50% of the injected mass from these two nozzles will disappear outside the fluid domain. In addition, although the experimentally measured temperature distribution on the endwindings [28] has a small level of asymmetry between the left part and the right part, it is deemed to be mainly caused by the asymmetric attaching positions of temperature sensors instead of the actual physics we are trying to simulate.

Since there is no experimentally measured data on the size distribution of spray droplets injected from the nozzles listed in Table 3, the correlation developed by Estes and Mudawar [59] is used for estimating their Sauter mean diameters.

$$\frac{D_{32}}{D_0} = 3.67[We_{D0}^{1/2} Re_{D0}]^{-0.259} \tag{27}$$

where We_{D0} and Re_{D0} are defined on the basis of the nozzle diameter and the nozzle pressure drop, $\frac{\rho_g(2\Delta P/\rho_l)D_0}{\sigma}$, $\frac{\rho_l(2\Delta P/\rho_l)^{1/2}D_0}{\mu_l}$. The calculated SMD is roughly 80 μm. This value is substituted in Eq. (13) to get the characteristic diameter, which is approximately 100 μm. Then the initial size of actual droplets injected into the fluid domain of the simulation follows the Rosin-Rammler distribution, Eq. (12), based on this obtained characteristic diameter, namely, the diameter for the spray droplets in each parcel is sampled from this Rosin-Rammler distribution.

Again, the heat generation in the hairpin endwindings is deactivated, viz., their surface heat flux is set to 0 W/(m^2 K), before the spray droplets reach them, for preventing their wall temperature values from reaching an unrealistic high value at the beginning. All the simulations were run in ANSYS Fluent R2021R2 on the high-performance computer (HPC) Tetralith located in the national supercomputer center at Linköping University. Each case was computed with 64 cores of Intel Xeon Gold 6130 CPU, and 181.5 GB RAM for approximately 120 h on average.

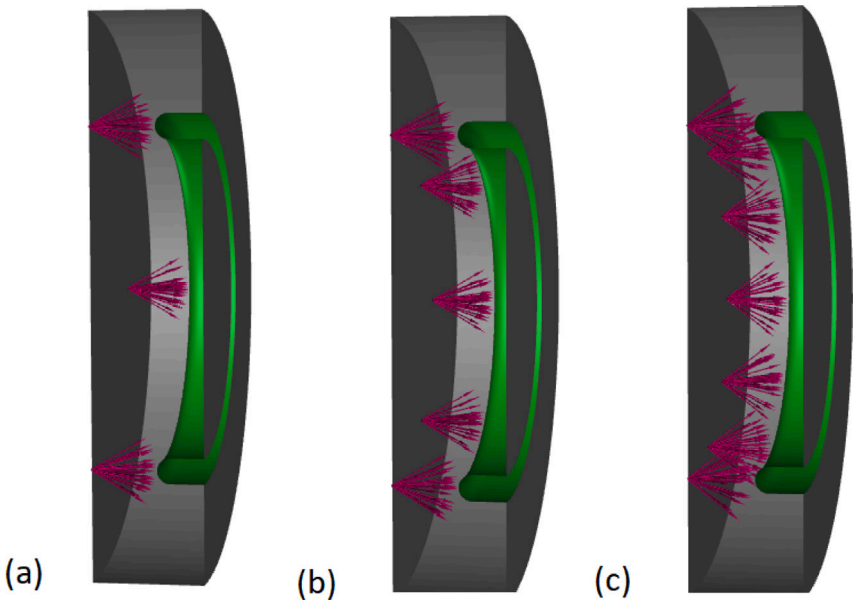

Fig. 3. Positions of spray nozzles (a) 4-nozzle case; (b) 8-nozzle case; (c) 12-nozzle case.

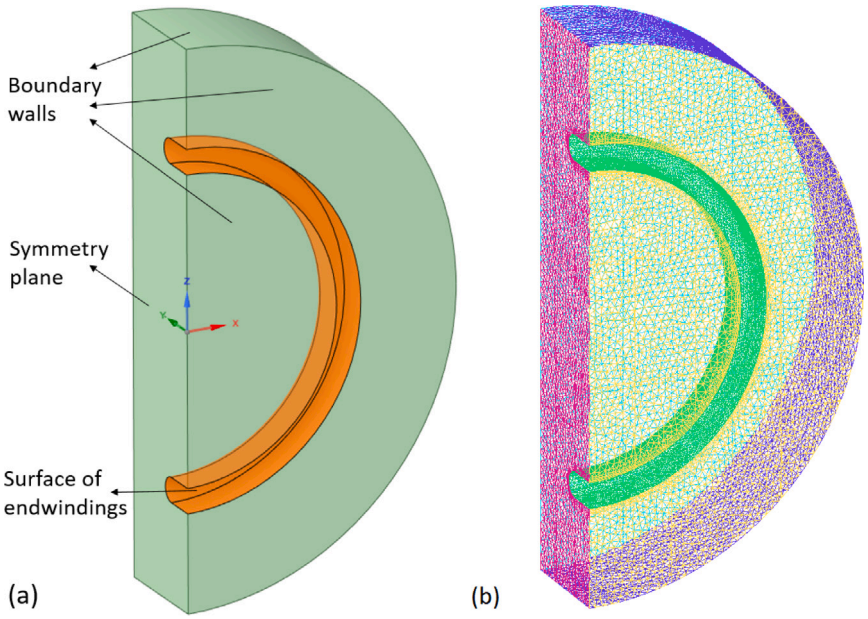

Fig. 4. Simplified geometry of endwindings (a) Geometry of fluid domain; (b) Mesh.

5. Analysis of different aspects in the simulation settings

There are many parameters and options involved in simulating this spray cooling process. A thorough study has been done to investigate their influence on the final results.

5.1. Check of reaching steady-state

Ensuring the solution has reached its steady-state is much more difficult for the present work than in previous research because there are two different time scales involved in the simulation of the aforementioned spray cooling configuration for a vertical-oriented object. One is related to the impact of spray droplets onto the thin liquid film accumulated on the surfaces of endwindings, the other is related to the dripping flow of this thin liquid film due to gravity. The former one is rather quick, usually on the magnitude of milliseconds or even microseconds [61]; while the latter one is much slower, usually on the magnitude of seconds or even minutes [62]. Both of these physics mechanisms are important in determining the heat transfer performance of this particular spray cooling process, with the former one playing its role in the zones directly under the nozzles, and the latter one mainly in the remained zones. Hence, it is necessary to take them into account simultaneously in the solution, by using a similar small time step but a much longer simulation time compared to other commonly adopted spray cooling designed for horizontal-oriented objects [23]. Nevertheless, it is shown in Fig. 5 that the curves of monitored wall temperature and wall-film thickness of the surface of endwindings become flat near 100 000 iterations, namely, 2 s. This is corroborated by the change of wall-film coverage contours in Fig. 6. The dry patches between the zones directly under the nozzles shrink gradually with the time marching. As more and more wall-film parcels enter the cells in these dry patches, these areas are transformed from

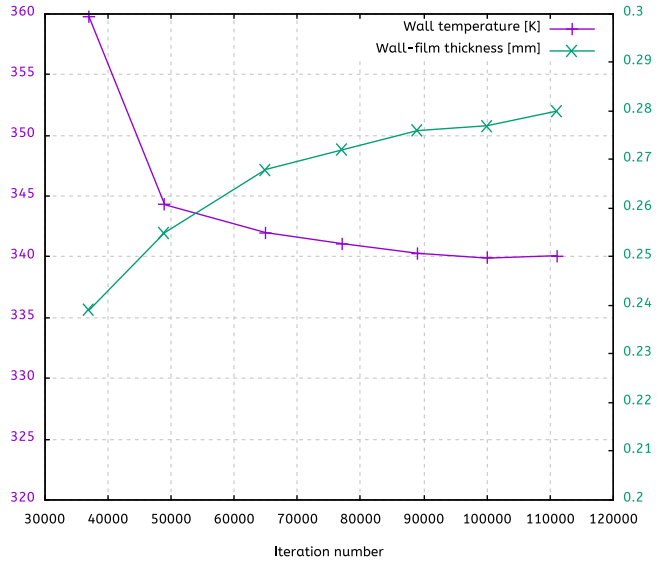

Fig. 5. Monitoring of wall temperature and wall-film thickness of the surface of endwindings during the solution.

partially wetted to fully wetted by the thin liquid film. When the surface of endwindings has already been fully covered after 2 s. Therefore, the solution is deemed to reach steady-state after 100 000 iterations and all later cases in this work are calculated until 100 000 iterations.

5.1.1. Comparison between the liquid film thickness and the boundary layer thickness

From the enlarged view of the velocity vectors near the surface of endwindings, the characteristic value for air velocity is found to be around 15 m/s. Together with the radial width 13.5 mm of the endwindings as the characteristic length, they are used to calculate the air Reynolds number, $\frac{\rho_g u_g L_{wd}}{\mu_g}$. As mentioned in Section 2.1, the spraying is a turbulent process, hence according to the relationship [63]

$$\delta = 0.37 \frac{L_{wd}}{Re_g^{1/5}}, \tag{28}$$

the turbulent air velocity boundary layer thickness is estimated to be 0.75 mm. The turbulent air thermal boundary layer thickness is approximately the same as its velocity boundary layer thickness [63]. While the thin oil film thickness over the surface of the endwindings, its distribution will be later in Fig. 19, ranges from 0.15 mm at the spots directly under the spray nozzles, to 0.40 mm at other spots. Clearly, the liquid film thickness is smaller than the boundary layer thickness, justifying the usage of the Realizable k-ϵ turbulence model [44] in combination with the standard wall function [64] for simulating the continuous gas phase.

5.2. Grid independence

It is important to ensure that the simulation results do not dependent on the grid numbers of the mesh. Three meshes, with 150k, 300k, and 500k cells are prepared in the same way only with the minimum element size altered. All three meshes adopt five layers of prism grids to adjust the y+ values at the wall of endwindings, in order to make them above 30. Fig. 7 indicates that the 150k cells case has a relatively large deviation in wall temperature and wall-film thickness from two other cases. However, the differences in wall temperature and wall-film thickness between the 300k cells case and the 500k cells cases are quite small, less than 0.5 K and 0.01 mm, respectively, and there are no visible distinguishable patterns or any unrealistic hot spot in their wall temperature and wall-film thickness contours, as seen in the supporting information of this paper. Hence, it is judged that the simulation results do not depend on the grid numbers of the mesh as long as its cell numbers are larger than 300k. Conservatively, the 500k cells mesh is used in all later cases of this work.

Table 4
Simulation results with different stream numbers for each spray injector.

Stream numbers	Averaged wall temperature [K]	Averaged wall-film thickness [mm]	Averaged wall-film velocity [m/s]
2	339	0.274	0.22
5	339	0.278	0.23
10	340	0.277	0.22
20	339	0.278	0.23
50	340	0.277	0.22
Stream numbers	**Total HTC [W/(m^2 K)]**	**Ununiformness of wall temperature [%]**	**Ununiformness of wall-film thickness [%]**
2	503	2.9	47.0
5	510	2.9	48.6
10	499	2.9	48.0
20	520	2.7	51.1
50	503	1.5	46.9

5.3. Influence of stream numbers

The stream numbers set for each spray injector represent the number of parcels used to model the spray droplets injected every DPM iteration. It is the dominating parameter that determines the computing time since most of the computing time is spent on the Lagrangian part of the solver instead of the Eulerian part. Decreasing the particle stream number from 50 to 2 greatly speeds up the computation, from approximately 200 h to merely 10 hours! As shown in Fig. 8, both the numbers of free spray parcels in the fluid domain and the wall-film parcels on the surface of endwindings are significantly reduced.[1] Fortunately, the simulation results for area-weighted averaging quantities do not differ more than the last effective digit according to the upper half of Table 4. Though sparser for the lower stream number cases, the DPM velocity vectors exhibit similar patterns no matter what stream number is chosen in the simulation. Moreover, there are no distinguishable patterns in other contours for different quantities on the surface of endwindings in the supporting information, either. Therefore, a low stream number, e.g. 5, is recommended as an initial setting for simulating the spray cooling process in similar scenarios to cut down the computing time. Of course, a stream number independence check is always welcome. Such stream number is much smaller compared to the stream number, say, 600 [65], used in the simulation of the fuel atomization process. It is reasonable because the injection of coolant spray is a continuous action and lasts all along the simulation time, while the injection of fuel is just a pulse that lasts a few microseconds. Hence, when simulating the spray cooling process, there would still be enough parcels to stochastically describe the spray in the long run, even with a very small stream number for each spray injector.

5.4. Influence of splashing submodel

As mentioned in the supporting information, the splashing submodel of the Lagrangian wall-film model can be turned off by setting the number of splashed parcels to 0. This could help reduce the number of spray parcels in the fluid domain so as to further cut down the computing time. As revealed in Table 5, the total heat transfer coefficient and other area-weighted averaging quantities stay almost the same no matter whether the splashing submodel is turned on or off, though the wall temperature and wall-film thickness ununiformness are a little bit

[1] Their numbers are already reduced 50 times for clearer visualization.

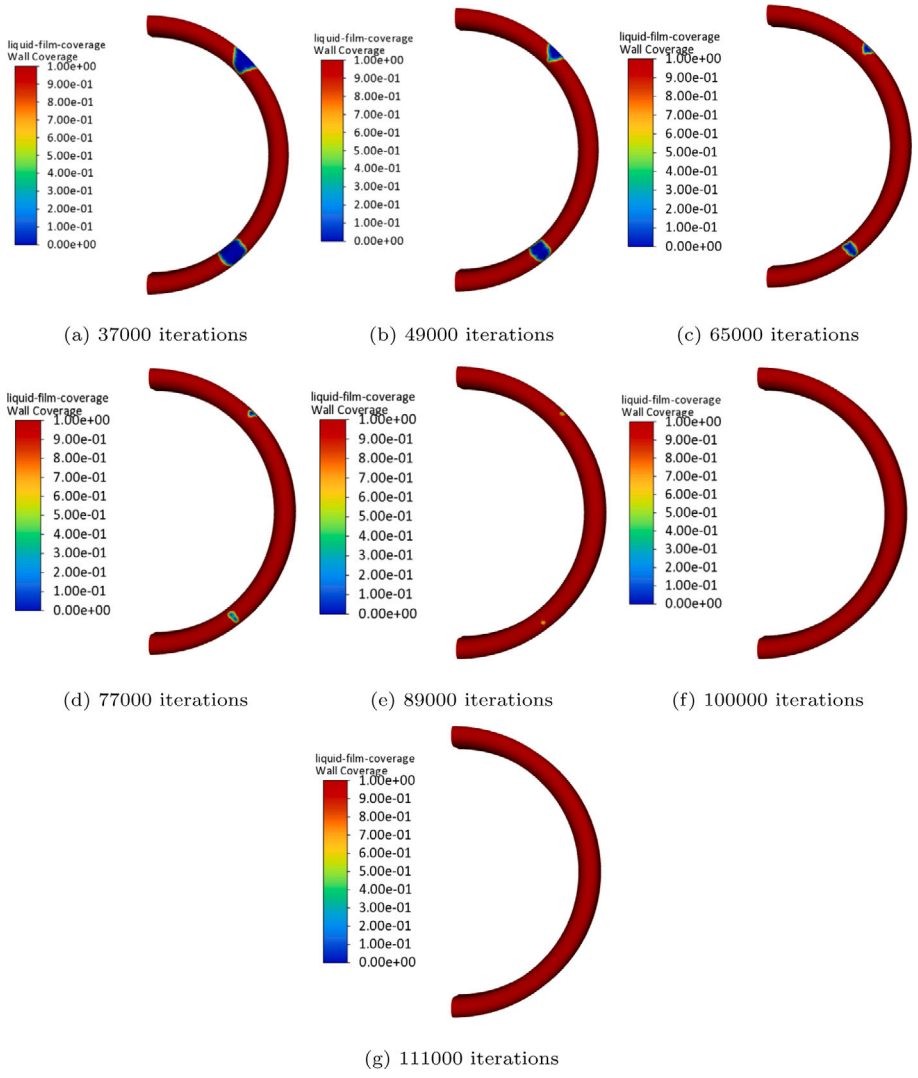

Fig. 6. Wall-film coverage contours at different iterations.

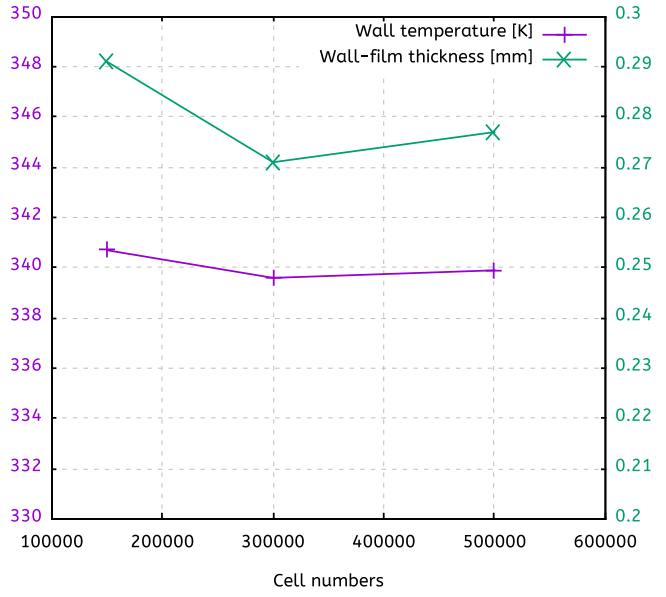

Fig. 7. Change of wall temperature and wall-film thickness of the surface of endwindings with varying cell numbers.

higher for the case with splashing submodel turned on. Hence, it is concluded here that the splashing phenomenon has a minor influence on the heat transfer performance of this spray cooling configuration. This can be explained as follows: The heat transferred from the surface of the endwindings is mostly removed by the thin liquid film flowing over it. The cooling capability of this wall-film is determined by its thickness and velocity. So, as long as the splashed droplets do not take away a significant mass fraction of the wall-film, or most of them fall back to become the wall-film again, splashing should not matter. This is affirmed by the summary of all DPM parcels. Less than 1% of the injected mass of coolant liquid ends up in the form of free spray parcels suspended in the fluid domain, the other 99% ends up in the form of wall-film parcels contributing to cooling the surface of endwindings. In view of this, the splashing submodel is turned off in all later cases of this work to reduce the extra computational cost and decrease the number of small spray droplets suspended in the fluid domain.

5.5. *Influence of breakup and collision submodels*

The pressure of air in the end cap region of electric machines is barely 1 bar, which leads to the much weaker secondary atomization process of spray droplets [66] than in the high-pressure chamber of internal combustion engines [67]. Hence, turning on the secondary breakup submodel [46] should have little influence on the spray cooling process. This inference is corroborated by the results in Table 6.

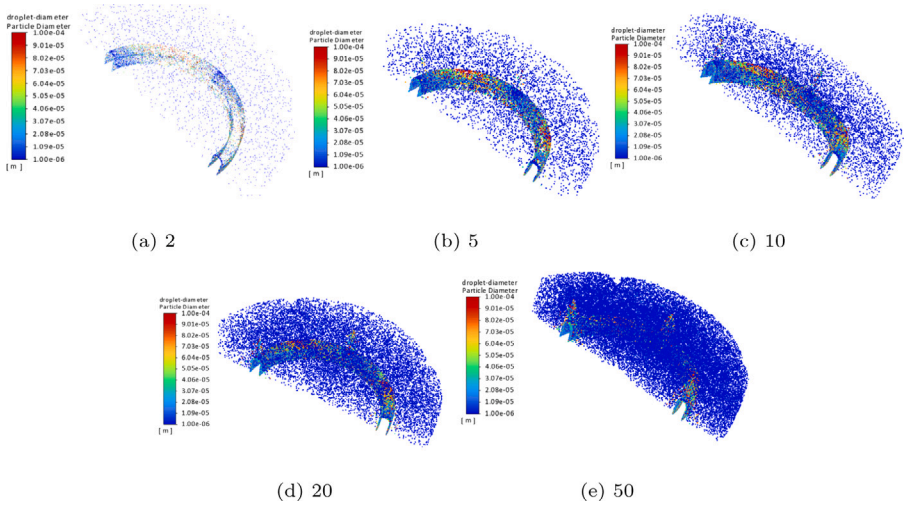

Fig. 8. Particle traces colored by droplet diameters for different particle streams.

Table 5
Simulation results with splashing turned on/off.

Splashing submodel	Averaged wall temperature [K]	Averaged wall-film thickness [mm]	Averaged wall-film velocity [m/s]
Off	340	0.277	0.22
On	340	0.279	0.23
Splashing submodel	Total HTC [W/(m^2 K)]	Ununiformness of wall temperature [%]	Ununiformness of wall-film thickness [%]
Off	503	2.9	48.6
On	510	2.9	53.0

On the contrary, it seems that the inclusion of the stochastic collision model [47] would deteriorate both the heat transfer performance of the spray cooling and undermine the uniformness of the wall temperature and wall-film thickness. But the heated endwindings surface where the spray droplets hit on sits distantly from the nozzle outlet, at least tens of nozzle diameters, in the current configuration of spray cooling for electric machines. The frequency of collisions among spray droplets should be low there and not influence the results that much. After a further inspection of the contours of the wall-film temperature, it is found that, in the case with the stochastic collision submodel turned on, there is a hot spot, circled black in Fig. 9, located in the lower part of the endwindings. The wall-film temperature in this region reaches an extraordinarily high value compared to its neighborhood, which becomes the cause of the higher averaged wall temperature and the significantly worse uniformness of wall temperature. It is actually close to a completely dried area as can be seen from its corresponding wall-film thickness contours in the supporting information. Such a phenomenon is highly unlikely to occur in reality and is suspected to be caused by the nature of the Lagrangian wall-film model: It computes the liquid film temperature in a specific grid by solving Eq. (18). If there are few spray parcels residing in the grid of some specific area over the endwindings, the sum of $m_{cp}c_{cp}$ in that grid becomes very small and makes T_{wp} very sensitive to the changes at the right-hand side of Eq. (18) – it is clearly a numerical artefact. Other methodologies, such as the Eulerian wall-film model [68], might be worth trying for fixing this issue to check whether the aforementioned inference, which deems the collision effect of spray droplets is a relatively unimportant factor, is true or not. Besides, the stochastic collision model is very computationally expensive, so it is kept turned off for all other simulation cases.

5.6. Influence of including the effect of heat conduction in the endwindings

The stator windings in electric machines are composed of copper conductors, thin round wires for randomly wound windings or thick rectangular wires for hairpin windings, and an insulation layer coated on them, usually made of lacquer [69]. The effect of heat conduction in them on the spray cooling heat transfer performance on endwindings can be modeled by using shell conduction layers on their solid wall surface. Cases with one shell conduction layer for only the copper conductors and two shell conduction layers for the copper conductors and the insulation layer, respectively, are both tried. The lower part of Table 7 demonstrates that the wall temperature distribution becomes more uniform with shell conduction layers modeled. But this is probably not realistic. It is just caused by adopting the simplified geometry model in the present work, which ignores the air gap separation between endwindings extended from different stator slots. Whereas, other quantities, like total heat transfer coefficient, change very little. Thus, as the effect of heat conduction in the endwindings will not actually affect the spray cooling heat transfer performance, no shell conduction layers are included in the model of later cases in this work.

5.7. Influence of Saffman lift force

Bai, et al. [70] have discovered that the Saffman lift force is of the same order of magnitude as the drag force in the near-wall region. Obviously, the trajectories of spray droplets near the surface of endwindings would be affected by the Saffman lift force. Hence, it is interesting to test whether the Saffman lift force would also affect the spray cooling heat transfer performance or not. The simulation results given in Table 8 and corresponding contours of different quantities in the supplemental information of this paper both manifest that the influence of the Saffman lift force has nearly negligible influence, so it is omitted in all later cases of this work.

5.8. Solving only the energy equation with frozen flow field

After certain injections of spray droplets reach the surface of the endwindings and a thin layer of the liquid film forms over it, the flow field of the air will reach a steady-state as the coupling source terms transferred from the dispersed liquid phase no longer vary. As a consequence, there is no need to continue solving the continuity and momentum equations of the air anymore, only the energy equation is solved in subsequent iterations. Table 9 compares the simulation results with all equations or only the energy equation solved for the continuous gas phase after a certain number of iterations, waiting for the flow field of air to reach its steady-state. The differences between all the metrics of these two cases are quite small, and no visible distinction can be observed in their corresponding contours of different quantities. Thus, whenever possible, this technique ought to be utilized to reduce the computing time further.

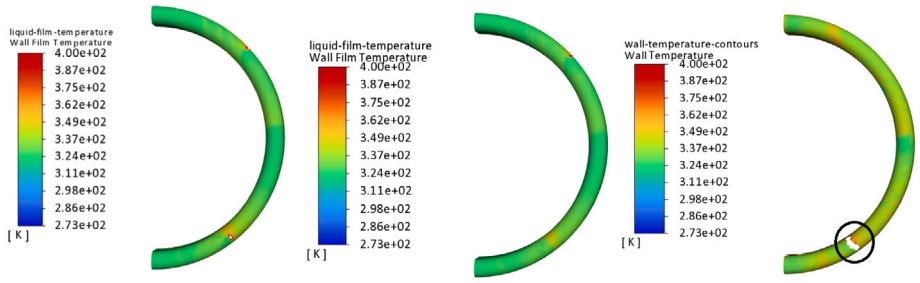

(a) No breakup or collision submodels (b) Only breakup submodel (c) Both breakup and collision submodels

Fig. 9. Wall-film temperature contours for cases with breakup or collision submodels.

Table 6
Simulation results for cases with breakup or collision submodels.

Submodels	Averaged wall temperature [K]	Averaged wall-film thickness [mm]	Averaged wall-film velocity [m/s]
No breakup or collision	340	0.277	0.22
Only breakup	339	0.277	0.22
Breakup and collision	344	0.299	0.41
Submodels	**Total HTC [W/(m^2 K)]**	**Ununiformness of wall temperature [%]**	**Ununiformness of wall-film thickness [%]**
No breakup or collision	503	2.9	47.0
Only breakup	525	2.9	52.3
Breakup and collision	420	42.4	57.8

Table 7
Simulation results with shell conduction layers added.

Shell conduction layers [–]	Averaged wall temperature [K]	Averaged wall-film thickness [mm]	Averaged wall-film velocity [m/s]
0	340	0.277	0.22
1	340	0.278	0.22
2	340	0.275	0.22
Shell conduction layers [–]	**Total HTC [W/(m^2 K)]**	**Ununiformness of wall temperature [%]**	**Ununiformness of wall-film thickness [%]**
0	503	1.5	46.9
1	506	0.3	51.8
2	508	0.4	44.0

Table 8
Simulation results with Saffman lift force turned on/off.

Saffman lift force	Averaged wall temperature [K]	Averaged wall-film thickness [mm]	Averaged wall-film velocity [m/s]
Off	339	0.278	0.23
On	339	0.279	0.22
Saffman lift force	**Total HTC [W/(m^2 K)]**	**Ununiformness of wall temperature [%]**	**Ununiformness of wall-film thickness [%]**
Off	510	2.9	48.6
On	522	2.9	47.6

Table 9
Simulation results with all equations or only the energy equation solved.

Equations solved	Averaged wall temperature [K]	Averaged wall-film thickness [mm]	Averaged wall-film velocity [m/s]
All	339	0.278	0.23
Only energy	340	0.279	0.23
Equations solved	**Total HTC [W/(m^2 K)]**	**Ununiformness of wall temperature [%]**	**Ununiformness of wall-film thickness [%]**
All	510	2.9	48.6
Only energy	506	3.5	49.6

6. Parametric study for design related choice and spray nozzles configurations

A lot of parameters in the operating conditions or the configurations of spray nozzles could influence the heat transfer performance of the spray cooling process. Sensitivity analyses are performed with several representative ones here, for guiding the design of the spray cooling setup or the selection of suitable coolant liquids. Their varying ranges are summarized in Table 10.

Table 10
Varying ranges for parameters analyses of the spray cooling process.

Case numbers	Flow rate [L/min]	Droplet size [mm]	Distance between nozzles and endwindings [mm]	Nozzle numbers
1	2.99	0.061	35	4
2	3.45	0.061	35	4
3	3.92	0.061	35	4
4	4.33	0.061	35	4
5	3.92	0.005	35	4
6	3.92	0.010	35	4
7	3.92	0.100	35	4
7	3.92	1.000	35	4
8	3.92	0.061	5	4
9	3.92	0.061	15	4
10	3.92	0.061	25	4
11	3.92	0.061	35	8
12	3.92	0.061	35	12

6.1. Influence of oil flow rate

Flow rate has been proved many times in previous research about spray cooling [11] to be one of the principal operation conditions that affect the overall cooling performance. Table 11 shows the simulation results of varying the flow rate with the baseline configuration of

Table 11
Simulation results from the parametric analysis of varying the flow rate.

Flow rate [L/min]	Averaged wall temperature [K]	Averaged wall-film thickness [mm]	Averaged wall-film velocity [m/s]
2.99	354	0.261	0.16
3.45	346	0.273	0.19
3.92	339	0.278	0.23
4.33	339	0.277	0.28
Flow rate [L/min]	Total HTC [W/(m^2 K)]	Ununiformness of wall temperature [%]	Ununiformness of wall-film thickness [%]
2.99	306	16.1	56.7
3.45	396	11.0	53.8
3.92	510	2.9	48.6
4.33	537	2.1	45.5

spray nozzles. It indicates that a larger flow rate leads to a larger thickness and velocity of the thin liquid film flowing over the surface of endwindings, which makes it remove heat at a quicker rate, thus, giving rise to lower wall temperature and larger total HTC. Moreover, a larger flow rate can reduce the ununiformness of wall temperature and wall-film thickness, resulting in more spatially uniform cooling efficacy.

6.1.1. Comparison to the HTC correlations for multi-nozzle spray cooling

Two highly-cited HTC correlations [71,72] in the community of spray cooling research are adopted here to examine the validity of the simulation results. They are selected because they are specifically targeted at single-phase spray cooling heat transfer with the evaporation effect nearly zero, which is consistent with the situation in this work. Both of them are based on the size of the heated surface. Here the characteristic area is chosen to be the total surface area of endwindings, A_{ew}, and the characteristic length is chosen to be the diameter of endwindings, D_{ew}. The Jiang et al. [71] correlation is written as

$$Nu_{ew} = 9.75 Re_{ew}^{0.7} Pr_l^{1/3} \tag{29}$$

while the Tao et al. [72] correlation is written as

$$Nu_{ew} = 0.6751 Re_{ew}^{0.77} Pr_l^{0.84} \tag{30}$$

where the Nusselt and Reynolds numbers of endwindings are defined as

$$Nu_{ew} = \frac{h_{corr} D_{ew}}{k_l} \tag{31}$$

$$Re_{ew} = \frac{Q D_{ew}}{A_{ew} \nu_l} \tag{32}$$

Fig. 10 demonstrates that though these two HTC correlations give higher HTCs at lower flow rates and lower HTCs at higher flow rates than the simulated HTCs, all of them correctly predict the increasing trend of spray cooling HTC with increasing the flow rate of the coolant liquid, and their values correlate well. Therefore, the validity of simulation results is recognized by these two spray cooling HTC correlations.

6.1.2. Comparison to the multi-nozzle spray cooling on endwindings experimental results

Furthermore, the measured HTCs from the experiments done by Liu, et al. [28,31], which are the reference source of all the simulation settings in this work as aforementioned in Section 4, are adopted to validate the simulation results here. They also varied the flow rates of the coolant liquid at these corresponding values. Fig. 11 shows that the measured HTCs differ quite a lot from the simulation results. Two issues are supposed to be the causes for such a large discrepancy.

First, the so-called "wall temperature values" of endwindings are measured by thermocouples attached to their surface with a certain amount of thermal paste. However, the actual temperature values measured by this method might be an average value of the wall temperature of endwindings and the wall-film temperature. This is because

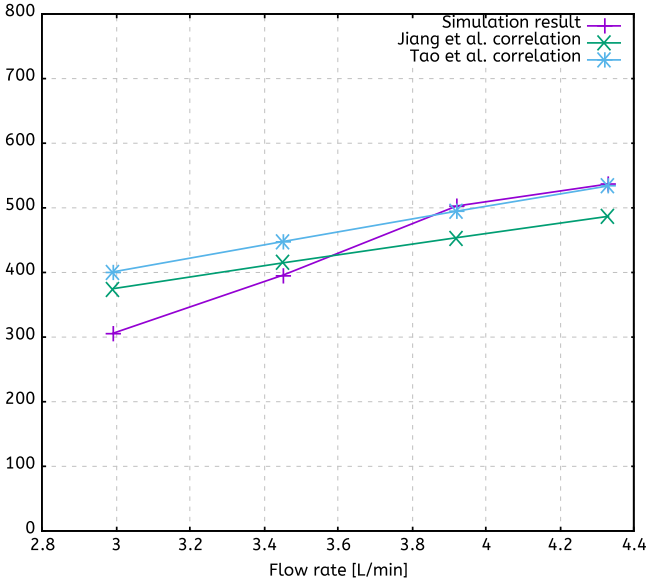

Fig. 10. Comparison of simulation results to Jiang et al. [71] and Tao et al. [72] spray cooling HTC correlations.

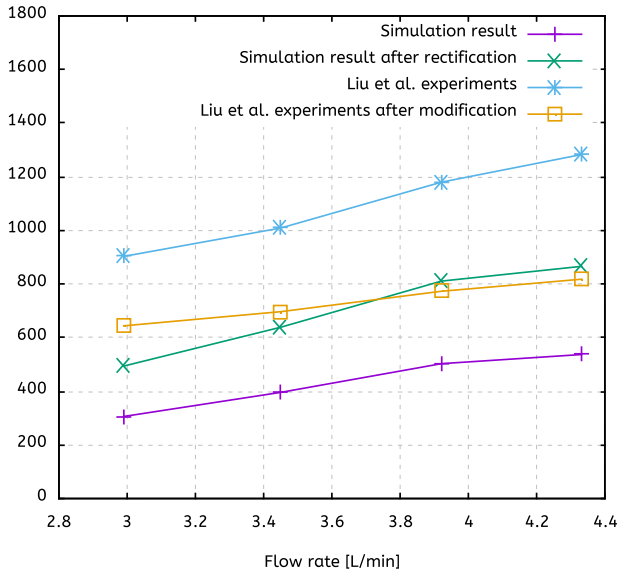

Fig. 11. Comparison of simulation results to Liu et al. [31] spray cooling HTC experimental results.

the thermal paste layer between those thermocouples and the wall of endwindings might be thicker than the thin liquid film flowing over the surface of endwindings, which is barely around 0.3 mm according to the simulation results. It makes the sensor heads of thermocouples might even be above the wall-film, thus measuring an unknown weighted temperature between the wall temperature and the wall-film temperature values. As the latter one is roughly 10 °C lower than the former one, an overestimation of the total HTCs might occur. Therefore, the measured HTCs from the experiments [28,31] are modified by assuming the "wall temperature values" used by Liu, et al. are an average value of the real wall temperature of endwindings and the wall-film temperature.

Second, the simplification of the geometry for endwindings is believed to bring about a certain degree of underestimation for the simulated HTCs. As claimed by La Rocca et al. [58] in 2019, the heat dissipation rate predicted by using the simplified geometry for

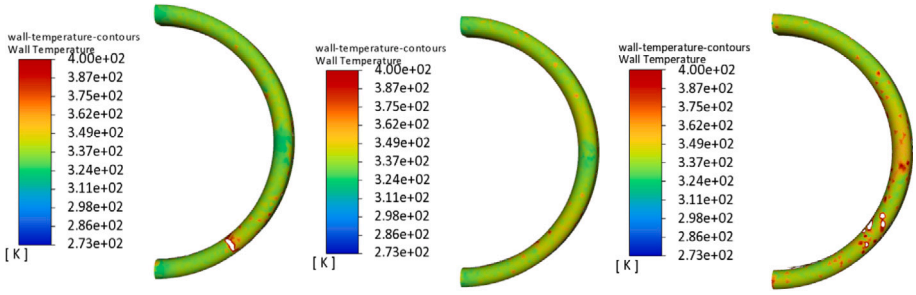

(a) 10 μm (b) 100 μm (c) 1000 μm

Fig. 12. Wall temperature contours for different droplet sizes.

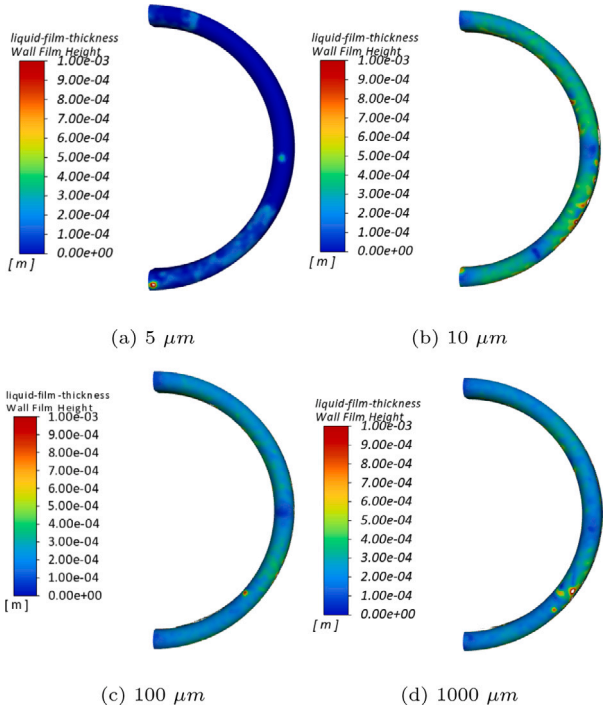

(a) 5 μm (b) 10 μm

(c) 100 μm (d) 1000 μm

Fig. 13. Wall-film thickness contours for different droplet sizes.

endwindings is 62.3% less than predicted by using the more realistic geometry for endwindings. Although they investigated the forced air convection heat transfer for the endwindings instead of the spray cooling setup that the present work focuses on, the mechanism of increase of the heat transfer performance, when changing from the simplified geometry for endwindings to a more realistic one, is the same. It is partly due to the increase of the heat exchange area per unit volume, partly due to the more complex vortex flow structure and higher tangential speed of air in the near wall region of the endwindings. Hence, the simulated HTCs should be rectified by a "geometrical factor" to account for the discrepancy in the heat transfer performance because of the adoption of the simplified geometry of endwindings. Here the number 62.3% is used as the initial guess for this "geometrical factor".

The modified experimentally measured HTCs and rectified simulated HTCs are also drawn in Fig. 11 and are found to be overlapped with each other. This signifies the simulation results could be validated by the experimental measurements after the proper modification or rectification of HTCs.

Table 12
Simulation results from the parametric analysis of varying the droplet size.

Droplet size [μm]	Averaged wall temperature [K]	Averaged wall-film thickness [mm]	Averaged wall-film velocity [m/s]
5[a]	–	0.047	0.02
10	339	0.350	0.56
100	341	0.274	0.35
1000	348	0.276	0.47
Droplet size [μm]	**Total HTC [W/(m² K)]**	**Ununiformness of wall temperature [%]**	**Ununiformness of wall-film thickness [%]**
5[a]	–	–	168.5
10	522	5.3	51.1
100	480	4.4	50.3
1000	368	9.2	60.1

[a]The averaged wall temperature of endwindings for the 5 μm case reaches an unrealistic high value. Hence, quantities related to it lose their meanings and are not given here.

6.2. Influence of droplet size

The size of spray droplets is another crucial parameter that affects the overall heat transfer performance of spray cooling [11]. It is linked to many other factors such as the pressure drop through the spray nozzles and requires complicated and expensive experimental apparatus such as laser Doppler diffraction to measure [52]. Hence, it is too difficult to vary the size of spray droplets independently in experiments, while this can be easily done in CFD simulation via setting the uniform distribution for spray droplets. The simulation results in Table 12 agree with the consensus in the community that smaller size of droplets leads to higher heat transfer performance of spray cooling [59]. It can be explained by the largest thickness and velocity of the wall-film of the 10 μm droplet diameter case, as shown in Figs. 13 and 14. Too large a droplet size will degrade the spatial uniformness. As shown in Fig. 12, obviously the 1000 μm droplet diameter case has more high-temperature spots. However, there is a lower bound. Decreasing the size of spray droplets to values smaller than this lower bound will not help enhance the cooling performance, on the contrary, it will significantly deteriorate the cooling performance. This is testified by the 5 μm droplet diameter case. It not only contains a huge dry surface area, as seen by the wall-film coverage contours in the support information of this paper, but also has much lower wall-film thickness and wall-film velocity on the wet surface of endwindings, as seen in Figs. 13(a) and 14(a). The summary of all DPM parcels reports that only half of the injected mass of coolant liquid ends up forming the thin liquid film over the surface of endwindings, affirmed by the sparser wall-film parcel traces in Fig. 15(a) compared to (b), (c) and (d). This is due to the too small inertia of the 5 μm diameter droplets. They do not follow the axial direction of endwindings to hit on their surface but are suspected to be drifted away because of the vortex structures generated by the wall-jet [73] in neighboring near-wall regions. It is made clear by comparing Fig. 16(a) to (b).

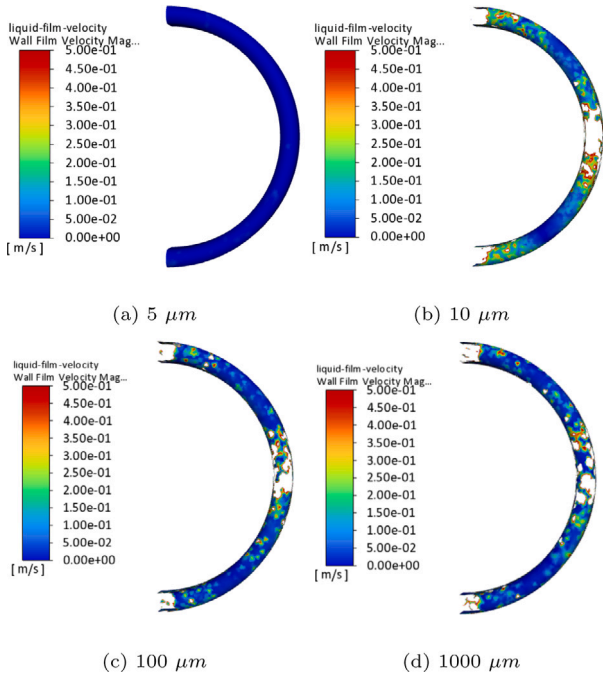

Fig. 14. Wall-film velocity contours for different droplet sizes.

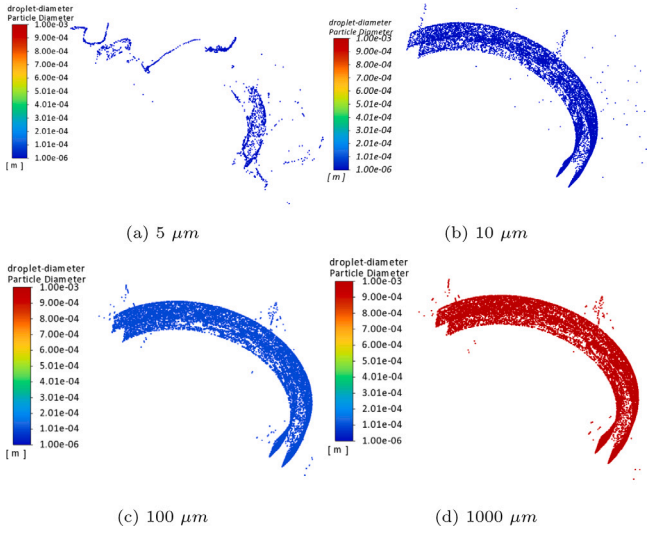

Fig. 15. Particle traces colored by droplet diameters for different droplet sizes.

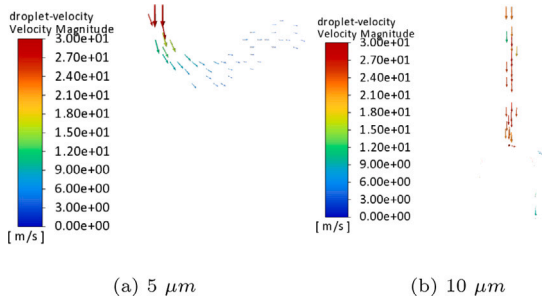

Fig. 16. DPM velocity vectors for different droplet sizes.

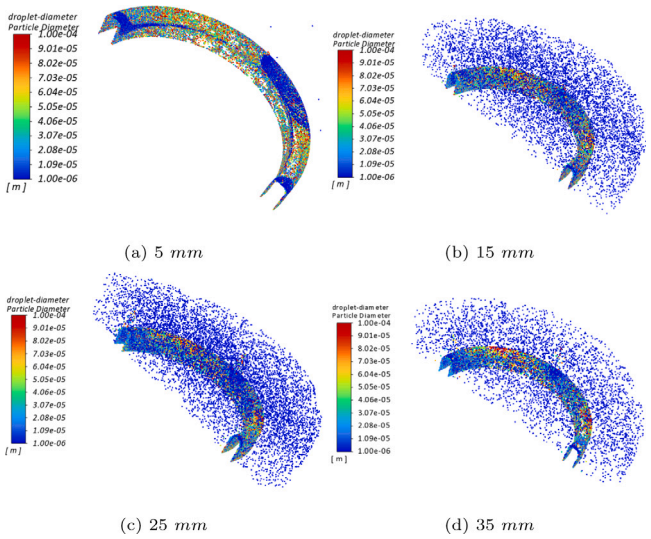

Fig. 17. Particle traces colored by droplet diameters for different spray heights.

Table 13
Simulation results from the parametric analysis of varying the distance between the nozzles and endwindings.

Distance [mm]	Averaged wall temperature [K]	Averaged wall-film thickness [mm]	Averaged wall-film velocity [m/s]
5	338	0.338	0.57
15	338	0.305	0.38
25	339	0.290	0.28
35	339	0.278	0.23
Distance [mm]	**Total HTC [W/(m^2 K)]**	**Ununiformness of wall temperature [%]**	**Ununiformness of wall-film thickness [%]**
5	548	3.3	52.4
15	545	3.0	49.5
25	532	2.7	48.6
35	510	2.9	48.6

6.3. Influence of distance between nozzles and endwindings

The distance between nozzles and endwindings is one of the vital parameters for configurations of spray nozzles that affects the overall cooling performance. Previous research [74] has discovered that there exists an optimum value for spray height under a specific operating condition. The simulation results of varying it are given in Table 13. It demonstrates that the thickness and velocity of wall-film increase with decreasing the spray height, which results in lower wall temperature of endwindings and higher total HTC. However, the ununiformness of wall temperature and wall-film thickness becomes more severe with decreasing the spray height, too. A distinct feature for the 5 mm spray height case is the complete elimination of small size droplets suspended in the fluid domain, as shown in Fig. 17(a) compared to 17(b), (c) and (d). This is suspected to be caused by the vanish of vortex structures in the near wall region, due to the limited space between the injector and the surface of endwindings.

6.4. Influence of nozzle numbers

Fig. 3(b) and (c) illustrate the arrangement of positions for 8 and 12 spray nozzles over the endwindings. For a fair comparison, the total flow rate of coolant liquid is fixed. Hence, the injected velocity of spray droplets for more nozzle numbers case is proportionally decreased, as shown in Fig. 18. The simulation results for all three configurations of spray nozzles are given in Table 14. It is found that the wall-film increases with more nozzles used, as clearly seen in Fig. 19, while the wall-film velocity decreases with more nozzles used, which can be seen

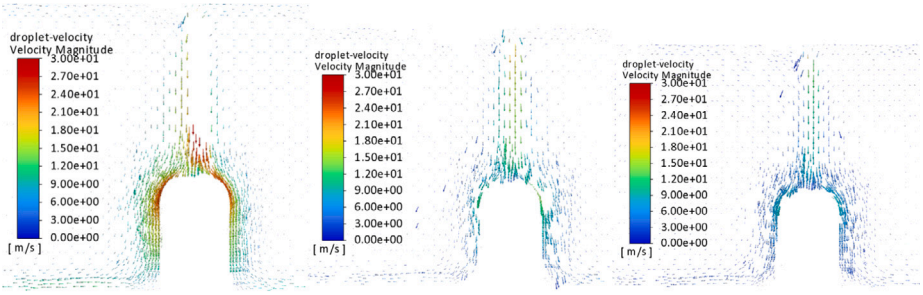

Fig. 18. DPM velocity vectors for different nozzle numbers.

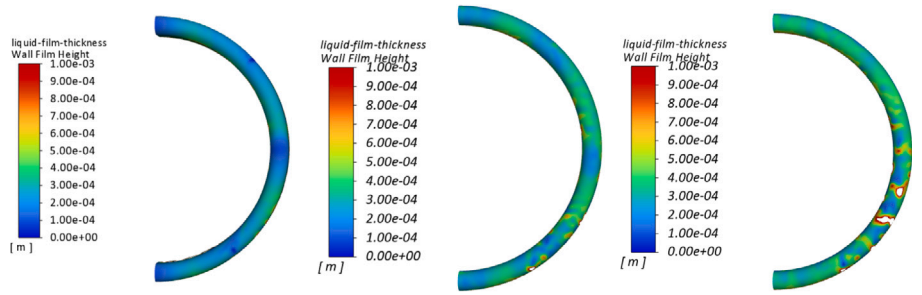

Fig. 19. Wall-film thickness contours for different nozzle numbers.

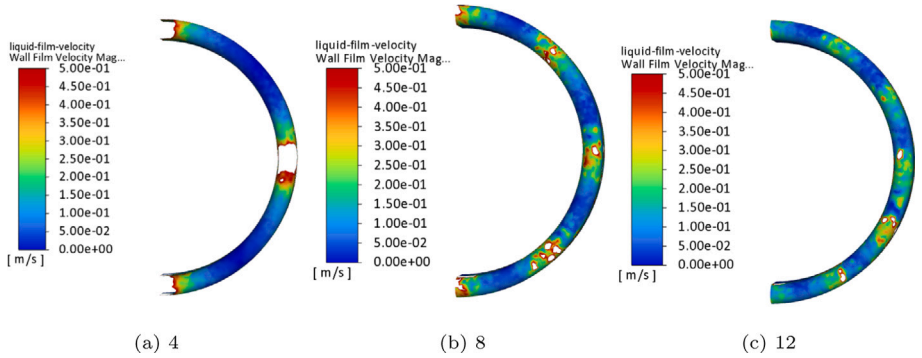

Fig. 20. Wall-film velocity contours for different nozzle numbers.

in Fig. 20 and is related to the decrease of the injected velocity of spray droplets when more spray nozzles are used. The combination of these two effects results in higher heat transfer performance, but opposite to the intuition, worse spatial wall temperature, and wall-film thickness uniformness. Evidently, extra caution is needed in selecting the optimal number of nozzles for the designer of such a spray cooling setup if the total flow rate of coolant liquid is fixed.

7. Summary and conclusions

This work investigates the heat transfer characteristics of spray cooling on endwindings of electric machines via the CFD simulation for a simplified geometrical model. The recommended settings are: 1. Set as few stream numbers as possible (e.g., 5 as a first try) for each spray injector as long as the accuracy of the computed results is preserved. This was shown to significantly cut down the computational cost; 2. Only solve the energy equation for the air (frozen velocity fields) when its flow field reaches the steady-state, for speeding up simulation; 3.

Table 14
Simulation results from the parametric analysis of varying the spray height.

Nozzle numbers [–]	Averaged wall temperature [K]	Averaged wall-film thickness [mm]	Averaged wall-film velocity [m/s]
4	339	0.278	0.23
8	339	0.349	0.17
12	338	0.404	0.15
Nozzle numbers [–]	**Total HTC [W/(m^2 K)]**	**Ununiformness of wall temperature [%]**	**Ununiformness of wall-film thickness [%]**
4	510	2.9	48.6
8	534	3.2	48.4
12	540	4.4	55.4

Since the splashing after the spray droplets impact on the wall/wall-film, the secondary atomization of the spray droplets, the effect of heat conduction in the endwindings, and the Saffman lift force have nearly

negligible influence on the cooling performance, these submodels can be turned off.

In order to achieve the best heat transfer performance of spray cooling on the endwindings, sensitivity analyses are done for parameters related to design choice and the configuration of the spray nozzles. It is found: 1. Around 75% increase of the total HTC and 8 times decrease of the ununiformness of wall temperature can be achieved by increasing around half the flow rate of the coolant liquid. Such performance enhancement is due to the thicker and faster thin liquid film flowing over the surface of endwindings produced by the larger mass flow rate. Furthermore, the predicted HTCs are validated with two correlations and rectified experimentally measured data; 2. Reducing the size of spray droplets leads to a larger total HTC and a more uniform distribution of wall temperature. But it needs to be kept above a lower bound, which is found to be between 5 μm and 10 μm of the droplet diameter; 3. Reducing the distance between nozzles and endwindings from 35 mm to 5 mm gives a 7% larger total HTC at the expense of slightly deteriorating the uniformness of wall temperature. In addition, all the tiny droplets suspended in the fluid domain observed in large distance cases are eliminated for the lowest distance case; 4. Increasing the nozzle number from 4 to 12 results in a 6% larger total HTC, even with the total flow rate of coolant liquid fixed.

Declaration of competing interest

The authors declare that they have no known competing financial interests or personal relationships that could have appeared to influence the work reported in this paper.

Data availability

Data will be made available on request.

Acknowledgments

This work is financially supported by the STandUP for Energy project. The authors are grateful to Prof. Luca Brandt, who kindly provides the HPC access via the project “Large-scale Simulations in Complex Flows” (SNIC 2022/1-38) and Prof. Chris Gerada, Dr. David Staton, Dr. Yew Chuan Chong who kindly provide their experimentally measured data.

Appendix A. Supplementary data

Supplementary material related to this article can be found online at https://doi.org/10.1016/j.applthermaleng.2023.121281.

References

[1] M. Popescu, J. Goss, D.A. Staton, D. Hawkins, Y.C. Chong, A. Boglietti, Electrical vehicles - Practical solutions for power traction motor systems, IEEE Trans. Ind. Appl. 54 (3) (2018) 2751–2762.
[2] B. Sarlioglu, C.T. Morris, More electric aircraft: Review, challenges, and opportunities for commercial transport aircraft, IEEE Trans. Transp. Electrif. 1 (1) (2015) 54–64.
[3] IEA, Global EV Outlook 2022, 2022, https://www.iea.org/reports/global-ev-outlook-2022.
[4] S. Nuzzo, D. Barater, C. Gerada, P. Vai, Hairpin windings: An opportunity for next-generation E-motors in transportation, IEEE Ind. Electron. Mag. (2021).
[5] N. Bianchi, G. Berardi, Analytical approach to design hairpin windings in high performance electric vehicle motors, in: 2018 IEEE Energy Conversion Congress and Exposition (ECCE), IEEE, 2018, pp. 4398–4405.
[6] W. Cai, D. Fulton, C.L. Congdon, Multi-set rectangular copper hairpin windings for electric machines, 2005, U.S. Patent 6, 894, 417.
[7] J.D. Kelly, 2016 - 2022 Prius, prius prime transaxle - P610 deep dive (P710, P810 similar), 2017, https://www.youtube.com/watch?v=-dHeRJdrnI8.
[8] C.-C. Chang, Y.-F. Kuo, J.-C. Wang, S.-L. Chen, Air cooling for a large-scale motor, Appl. Therm. Eng. 30 (11–12) (2010) 1360–1368.
[9] A. Acquaviva, O. Wallmark, E.A. Grunditz, S.T. Lundmark, T. Thiringer, Computationally efficient modeling of electrical machines with cooling jacket, IEEE Trans. Transp. Electrif. 5 (3) (2019) 618–629.
[10] C. Dong, Y. Qian, Y. Zhang, W. Zhuge, A review of thermal designs for improving power density in electrical machines, IEEE Trans. Transp. Electrif. 6 (4) (2020) 1386–1400.
[11] G. Liang, I. Mudawar, Review of spray cooling–Part 1: Single-phase and nucleate boiling regimes, and critical heat flux, Int. J. Heat Mass Transfer 115 (2017) 1174–1205.
[12] S. Khandekar, G. Sahu, K. Muralidhar, E.Y. Gatapova, O.A. Kabov, R. Hu, X. Luo, L. Zhao, Cooling of high-power LEDs by liquid sprays: Challenges and prospects, Appl. Therm. Eng. 184 (2021) 115640.
[13] G. Sahu, S. Khandekar, K. Muralidhar, Thermal characterization of spray impingement heat transfer over a High-Power LED module, Therm. Sci. Eng. Prog. 32 (2022) 101332.
[14] M.R. Panão, A.M. Correia, A.L. Moreira, High-power electronics thermal management with intermittent multijet sprays, Appl. Therm. Eng. 37 (2012) 293–301.
[15] K. Oliphant, B. Webb, M. McQuay, An experimental comparison of liquid jet array and spray impingement cooling in the non-boiling regime, Exp. Therm Fluid Sci. 18 (1) (1998) 1–10.
[16] L. Lin, R. Ponnappan, Heat transfer characteristics of spray cooling in a closed loop, Int. J. Heat Mass Transfer 46 (20) (2003) 3737–3746.
[17] X. Gao, R. Li, Effects of nozzle positioning on single-phase spray cooling, Int. J. Heat Mass Transfer 115 (2017) 1247–1257.
[18] M. Jafari, S. Jowkar, M. Morad, Low flow rate spray cooling by a flow blurring injector, Int. Commun. Heat Mass Transfer 122 (2021) 105168.
[19] K. Ali, R. Amna, M.U. Rashid, M.I. Malik, K. Kim, An investigation of the influence of surface roughness, water quality and nozzle on spray cooling of Aluminum alloy 6082, Therm. Sci. Eng. Prog. 10 (2019) 280–286.
[20] J.-X. Wang, Y.-Z. Li, M.-L. Zhong, H.-S. Zhang, Investigation on a gas-atomized spray cooling upon flat and micro-structured surfaces, Int. J. Therm. Sci. 161 (2021) 106751.
[21] S. Chakraborty, I. Sarkar, A. Roshan, S.K. Pal, S. Chakraborty, Spray cooling of hot steel plate using aqueous solution of surfactant and polymer, Therm. Sci. Eng. Prog. 10 (2019) 217–231.
[22] A.S. Salman, N.M. Abdulrazzaq, A. Tikadar, S.K. Oudah, J.A. Khan, Parametric study of heat transfer characteristics of enhanced surfaces in a spray cooling system: An experimental investigation, Appl. Therm. Eng. 183 (2021) 115824.
[23] A. Zeraatkardevin, S. Jowkar, M.R. Morad, X. Shen, A three dimensional simulation of spray cooling and its evaporating liquid film generated on patterned surfaces, Int. J. Multiph. Flow. (2022) 104174.
[24] X. Wang, B. Li, D. Gerada, K. Huang, I. Stone, S. Worrall, Y. Yan, A critical review on thermal management technologies for motors in electric cars, Appl. Therm. Eng. 201 (2022) 117758.
[25] T. Davin, J. Pellé, S. Harmand, R. Yu, Experimental study of oil cooling systems for electric motors, Appl. Therm. Eng. 75 (2015) 1–13.
[26] D.H. Lim, S.C. Kim, Thermal performance of oil spray cooling system for in-wheel motor in electric vehicles, Appl. Therm. Eng. 63 (2) (2014) 577–587.
[27] M.H. Park, S.C. Kim, Thermal characteristics and effects of oil spray cooling on in-wheel motors in electric vehicles, Appl. Therm. Eng. 152 (2019) 582–593.
[28] C. Liu, Z. Xu, D. Gerada, J. Li, C. Gerada, Y.C. Chong, M. Popescu, J. Goss, D. Staton, H. Zhang, Experimental investigation on oil spray cooling with hairpin windings, IEEE Trans. Ind. Electron. 67 (9) (2019) 7343–7353.
[29] Y.C. Chong, J. Goss, M. Popescu, D. Staton, C. Liu, D. Gerada, Z. Xu, C. Gerada, Experimental characterisation of radial oil spray cooling on a stator with hairpin windings, in: The 10th International Conference on Power Electronics, Machines and Drives (PEMD), IET, 2020, pp. 879–884.
[30] C. Liu, D. Gerada, Z. Xu, Y.C. Chong, M. Michon, J. Goss, J. Li, C. Gerada, H. Zhang, Estimation of oil spray cooling heat transfer coefficients on hairpin windings with reduced-parameter models, IEEE Trans. Transp. Electrif. 7 (2) (2020) 793–803.
[31] C. Liu, Z. Xu, D. Gerada, F. Zhang, Y.C. Chong, M. Michon, J. Goss, C. Gerada, H. Zhang, Experimental investigation of oil jet cooling in electrical machines with hairpin windings, IEEE Trans. Transp. Electrif. 9 (1) (2022) 598–608.
[32] C. Beck, J. Schorr, H. Echtle, J. Verhagen, A. Jooss, C. Krüger, M. Bargende, Numerical and experimental investigation of flow phenomena in rotating step-holes for direct-spray-cooled electric motors, Int. J. Engine Res. 22 (5) (2021) 1731–1740.
[33] C.W. Hirt, B.D. Nichols, Volume of fluid (VOF) method for the dynamics of free boundaries, J. Comput. Phys. 39 (1) (1981) 201–225.
[34] T. Ha, D.K. Kim, Study of injection method for maximizing oil-cooling performance of electric vehicle motor with hairpin winding, Energies 14 (3) (2021) 747.
[35] S. Koshizuka, Y. Oka, Moving-particle semi-implicit method for fragmentation of incompressible fluid, Nucl. Sci. Eng. 123 (3) (1996) 421–434.
[36] A. La Rocca, A. Fregni, S. La Rocca, C. Gerada, Numerical thermal modelling of multiphase spray cooling of hairpin windings, in: 2020 International Conference on Electrotechnical Complexes and Systems (ICOECS), IEEE, 2020, pp. 1–5.

[37] A. La Rocca, T. Zou, M. Moslemin, D. Gerada, C. Gerada, A. Cairns, Thermal modelling of a liquid cooled traction machine with 8-layer hairpin windings, in: 47th Annual Conference of the IEEE Industrial Electronics Society (IECON), IEEE, 2021, pp. 1–6.
[38] W.A. Sirignano, Fluid dynamics of sprays: 1992 Freeman scholar lecture, J. Fluids Eng. 115 (3) (1993) 345–378.
[39] Eastman, Technical data sheet of turbo oil 2389, 2018.
[40] ASTM, D972 standard test method for evaporation loss of lubricating greases and oils, 2016.
[41] P. Canada, Vapor Pressure Of Lubricating Oil, 2023, https://lubricants.petro-canada.com/en-nl/lube-source-handbook/glossary-of-terms-and-conversion-tables/vapor-pressure-of-lubricating-oil.
[42] ANSYS, FLUENT V2022R1 theory guide, 2022.
[43] C. Cai, H. Liu, M. Jia, H. Yin, R. Xie, P. Yan, Numerical investigation on heat transfer of water spray cooling from single-phase to nucleate boiling region, Int. J. Therm. Sci. 151 (2020) 106258.
[44] T.-H. Shih, W.W. Liou, A. Shabbir, Z. Yang, J. Zhu, A new k-e eddy viscosity model for high reynolds number turbulent flows, Comput. & Fluids 24 (3) (1995) 227–238.
[45] J.K. Dukowicz, A particle-fluid numerical model for liquid sprays, J. Comput. Phys. 35 (2) (1980) 229–253.
[46] P.J. O'Rourke, A.A. Amsden, The Tab Method for Numerical Calculation of Spray Droplet Breakup, Tech. Rep., SAE Technical Paper, 1987.
[47] P.J. O'Rourke, Collective Drop Effects on Vaporizing Liquid Sprays (Ph.D. thesis), Princeton University, 1981.
[48] P.G. Saffman, The lift on a small sphere in a slow shear flow, J. Fluid Mech. 22 (2) (1965) 385–400.
[49] A. Gosman, E. Loannides, Aspects of computer simulation of liquid-fueled combustors, J. Energy 7 (6) (1983) 482–490.
[50] S. Morsi, A. Alexander, An investigation of particle trajectories in two-phase flow systems, J. Fluid Mech. 55 (2) (1972) 193–208.
[51] W. Ranz, Evaporation from drops, Parts I & II, Chem. Eng. Prog. 48 (1952) 141–146.
[52] A.H. Lefebvre, V.G. McDonell, Atomization and Sprays, second ed., CRC Press, 2017.
[53] P. O'rourke, A. Amsden, A particle numerical model for wall film dynamics in port-injected engines, SAE Trans. (1996) 2000–2013.
[54] D.W. Stanton, C.J. Rutland, Modeling fuel film formation and wall interaction in diesel engines, SAE Trans. (1996) 808–824.
[55] M.A. Friedrich, H. Lan, J. Wegener, J. Drallmeier, B.F. Armaly, A separation criterion with experimental validation for shear-driven films in separated flows, J. Fluids Eng. 130 (5) (2008).
[56] H. Liu, C. Cai, Y. Yan, M. Jia, B. Yin, Numerical simulation and experimental investigation on spray cooling in the non-boiling region, Heat Mass Transf. 54 (12) (2018) 3747–3760.
[57] J.P. Holman, Heat Transfer, tenth ed., McGraw Hill Higher Education, 2010.
[58] S. La Rocca, S.J. Pickering, C.N. Eastwick, C. Gerada, K. Rönnberg, Fluid flow and heat transfer analysis of TEFC machine end regions using more realistic end-winding geometry, J. Eng. 2019 (17) (2019) 3831–3835.
[59] K.A. Estes, I. Mudawar, Correlation of Sauter mean diameter and critical heat flux for spray cooling of small surfaces, Int. J. Heat Mass Transfer 38 (16) (1995) 2985–2996.
[60] G.H. Abdul-Majeed, N.B.A. Al-Soof, Estimation of gas–oil surface tension, J. Pet. Sci. Eng. 27 (3–4) (2000) 197–200.
[61] J. Breitenbach, I.V. Roisman, C. Tropea, From drop impact physics to spray cooling models: a critical review, Exp. Fluids 59 (3) (2018) 1–21.
[62] K. Meredith, A. Heather, J. de Vries, Y. Xin, A numerical model for partially-wetted flow of thin liquid films, WIT Trans. Eng. Sci. 70 (2011) 239–250.
[63] H. Schlichting, J. Kestin, Boundary Layer Theory, eightth ed., Springer, 2000.
[64] B. Launder, D. Spalding, The numerical computation of turbulent flows, Comput. Methods Appl. Mech. Engrg. 3 (2) (1974) 269–289.
[65] ANSYS, FLUENT V2022R1 tutorials, 2022.
[66] G. Faeth, L.-P. Hsiang, P.-K. Wu, Structure and breakup properties of sprays, Int. J. Multiph. Flow. 21 (1995) 99–127.
[67] R.D. Reitz, Modeling atomization processes in high-pressure vaporizing sprays, At. Spray Technol. 3 (4) (1987) 309–337.
[68] R. Schmehl, H. Rosskamp, M. Willmann, S. Wittig, CFD analysis of spray propagation and evaporation including wall film formation and spray/film interactions, Int. J. Heat Fluid Flow 20 (5) (1999) 520–529.
[69] T.A. Lipo, Introduction to AC Machine Design, John Wiley & Sons, 2017.
[70] C. Bai, A. Gosman, Development of methodology for spray impingement simulation, SAE Trans. (1995) 550–568.
[71] S. Jiang, V.K. Dhir, Spray cooling in a closed system with different fractions of non-condensibles in the environment, Int. J. Heat Mass Transfer 47 (25) (2004) 5391–5406.
[72] Y. Tao, X. Huai, L. Wang, Z. Guo, Experimental characterization of heat transfer in non-boiling spray cooling with two nozzles, Appl. Therm. Eng. 31 (10) (2011) 1790–1797.
[73] B. Asgari, E. Amani, An improved spray-wall interaction model for Eulerian-Lagrangian simulation of liquid sprays, Int. J. Multiph. Flow. 134 (2021) 103487.
[74] W.-L. Cheng, Q.-N. Liu, R. Zhao, H.-l. Fan, Experimental investigation of parameters effect on heat transfer of spray cooling, Heat Mass Transf. 46 (8) (2010) 911–921.